An Assessment of the Parameterization of Subgrid-Scale Cloud Effects on Radiative Transfer. Part II: Horizontal Inhomogeneity

NORMAN B. WOOD, PHILIP M. GABRIEL, AND GRAEME L. STEPHENS

Department of Atmospheric Science, Colorado State University, Fort Collins, Colorado

(Manuscript received 23 July 2004, in final form 5 January 2005)

ABSTRACT

The role of horizontal inhomogeneity in radiative transfer through cloud fields is investigated within the context of the two-stream approximation. Spatial correlations between cloud optical properties and the radiance field are introduced in the three-dimensional radiative transfer equation and lead to a two-stream model in which the correlations are represented by parameterizations. The behavior of the model is examined using simple single-layer single-column atmospheres. Positive correlations between extinction or scattering and the radiance field are shown to decrease transmission, increase reflection, and increase absorption within inhomogeneous media. The parameterization is used to evaluate the characteristics of inhomogeneous cloud fields observed by radar and lidar over a number of different locations and seasons, revealing that shortwave transfer is generally characterized by negative correlations between extinction and radiance, while longwave transfer is characterized by positive correlations. The results from this characterization are applied to the integration of an atmospheric general circulation model. Model surface temperatures are significantly affected, largely in response to changes in downwelling radiative fluxes at the surface induced by changes in cloud cover and water vapor distributions.

1. Introduction

Cloud fields are, by necessity, treated simplistically within the radiative transfer parameterizations of atmospheric general circulation models (AGCMs). In these one-dimensional parameterizations, the vertical arrangement of the cloudy portions of the model layers (i.e., overlap) is handled using empirical treatments intended to produce unbiased estimates of domain-mean fluxes and heating rates. Part I of this study (Stephens et al. 2004) examined the success of various schemes in achieving this objective. A further simplification is that the in-cloud optical properties are horizontally homogeneous.

Modeling and observational evidence suggests that treating clouds as horizontally homogeneous leads to significant errors in radiative transfer. Räisänen et al. (2003), using a broadband Monte Carlo code and in situ aircraft observations of marine stratus, found that assuming horizontally homogeneous cloud liquid water path and cloud droplet effective radius led to errors of up to 10 W m^{-2} in the net top-of-the-atmosphere solar flux. The clouds examined in that work had layer-mean liquid water paths ranging from 10 to 120 g m^{-2} with standard deviations ranging from about 30%–70% of the mean values. In contrast, several studies have suggested much greater horizontal variability in stratus clouds (Stephens 1978; Dong et al. 2002), and it seems likely that the errors induced by treating these clouds as horizontally homogeneous would be larger than those found by Räisänen et al.

Despite the potential significance of these errors, there has been very little theoretical development directly applicable to the two-stream radiative transfer formulations used in AGCMs. A number of studies have presented solutions that apply the independent column approximation (ICA) in a weighted fashion directly to the two-stream radiative transfer solution. Weights can be determined by prescribing an analytical form for the horizontal variation in the cloud optical properties (Cahalan et al. 1994; Barker 1996). This approach leads to rescaled values for the bulk optical properties of the medium, which can then be applied in a single-column calculation, but omits the explicit treatment of spatial correlations between the radiance field

Corresponding author address: Norman B. Wood, Department of Atmospheric Science, Colorado State University, Fort Collins, CO 80523.
E-mail: norm@atmos.colostate.edu

and cloud optical properties. These correlations have been demonstrated to be significant in shortwave transfer through inhomogeneous clouds (Gabriel and Evans 1996), and several modifications to the weighted two-stream approach have been presented (Oreopoulos and Barker 1999; Kato 2003) to treat elements of the correlations. Weights can also be determined by sampling a known or assumed distribution of cloud properties. The resulting profiles can be used to perform multiple single-column two-stream calculations that are then averaged in the ICA fashion. The computational burden can be reduced by associating each cloud sample with a particular radiative spectral interval [e.g., the Monte Carlo ICA of Pincus et al. (2003)], but this comes at a cost of introducing random noise into the radiative transfer results. The particular AGCM examined by Pincus et al. showed little sensitivity to the radiative noise.

A more fundamental approach explicitly introduces the horizontal variations of the radiance field and cloud optical properties into the three-dimensional equation of radiative transfer. Stephens (1988a,b) presented a general framework using this approach based on a spatial-scale hierarchy and closure, then demonstrated the application of this framework to the problem of two-stream radiative transfer without sources using first-order closures. Kobayashi (1991) applied the method described by Stephens, but in a fully multidimensional radiative transfer model, which was not intended for AGCM application. Anasimov and Fukshansky (1992) presented a related development in the context of stochastic radiative transfer that generalized the solution in terms of *N*th-order closure. Cairns et al. (2000) utilized a perturbative method to solve the radiative transfer equation subject to spatially varying cloud droplet number concentrations. This treatment led to renormalized values for droplet optical properties, which could then be used in two-stream radiative transfer calculations.

In this paper we demonstrate a complete two-stream radiative transfer parameterization, including longwave and shortwave radiative transfer with sources, that uses the spatial-scale approach of Stephens (1988b). We show that the assumption of horizontally homogeneous cloud optical properties produces significant biases in the calculated two-stream fluxes and heating rates typically required by AGCMs. We introduce a method for parametrically representing correlations between horizontally inhomogeneous extinction and scattering coefficients and the radiance field within the framework of standard two-stream radiative transfer. No appreciable, additional computational burden is incurred. Using radar and lidar observations made at a number of sites operated by the Atmospheric Radiation Measurement (ARM) Program, we show that the new method is able to better approximate the fluxes that would be found in atmospheres containing real, horizontally inhomogenous clouds and develop estimates of required parameters. The parameterization is applied in the integration of an AGCM and is shown to significantly alter the resulting climatology of the AGCM, suggesting that omitting the treatment of horizontal inhomogeneity introduces a significant artificial forcing.

2. The influence of horizontal inhomogeneity on domain-averaged fluxes and heating rates

The errors associated with subgrid-scale variability arise from both the parameterization of the vertical cloud structure (overlap) and the assumption of horizontal homogeneity within the cloud. Overlap errors were treated in Part I (Stephens et al. 2004) using approximately 2000 two-dimensional cloud fields, or domains, similar in size to AGCM columns. The domains were constructed from high-resolution Active Remotely Sensed Clouds Locations (ARSLC; Clothiaux et al. 2000) cloud radar and lidar measurements produced by the U.S. Department of Energy ARM Program. These same domains, each consisting of 1080 consecutive ARSCL profiles taken at 10-s intervals, are used in this study to evaluate errors associated with horizontal inhomogeneity. As before, the time domain is used as a proxy for the horizontal domain, the vertical resolution is degraded to be similar to that of an AGCM, and five locales are used: Nauru, southern Great Plains (SGP) summer, SGP winter, North Slope of Alaska (NSA) summer, and NSA winter.

To evaluate the significance of errors associated with horizontal inhomogeneity, three types of radiative flux calculations were performed for each domain:

1) Domain-averaged independent column approximation with horizontally inhomogeneous cloud water contents, $\overline{F}_{\mathrm{ICA,inhomog}}$.
2) Domain-averaged ICA with horizontally homogeneous cloud water contents, $\overline{F}_{\mathrm{ICA,homog}}$.
3) Plane-parallel calculations with parameterized overlap and horizontally homogeneous cloud water contents, F_{pp}.

In each layer of a domain, the homogeneous cloud water contents were computed as the means of the inhomogeneous, nonzero cloud water contents. Radiative transfer calculations were performed using BUGSrad (Stephens et al. 2001), a two-stream radiative transfer model that has been used in AGCMs, cloud-resolving models, and single-column models. For the purely

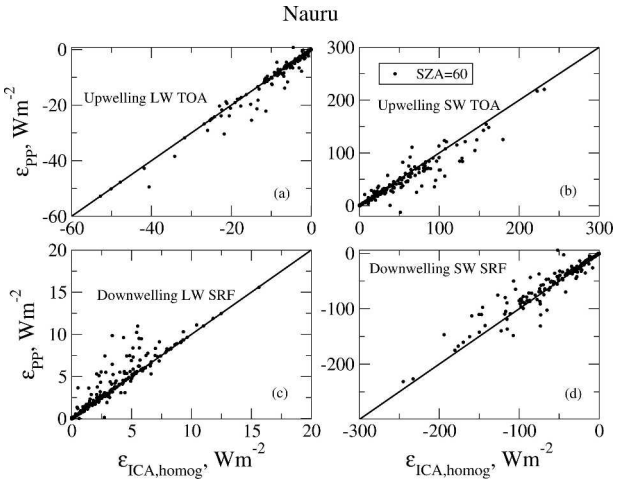

FIG. 1. Comparison of errors (W m^{-2}) due to overlap parameterization plus horizontal homogenization (vertical axes) with those due solely to horizontal homogenization (horizontal axes) for all Nauru domains for (a) upwelling longwave flux at TOA, (b) upwelling shortwave flux at TOA, (c) downwelling longwave flux at the surface, and (d) downwelling shortwave flux at the surface.

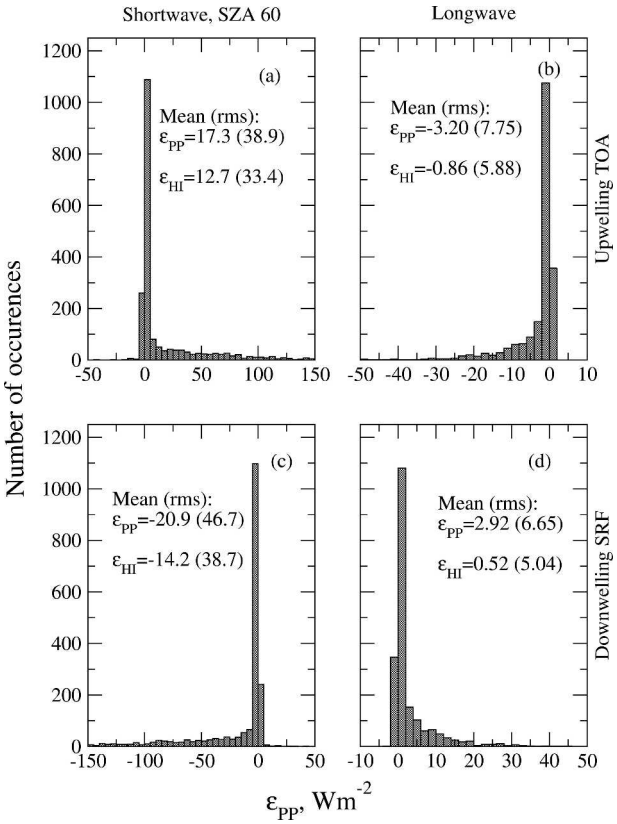

FIG. 2. Histograms of errors due to treating inhomogeneous clouds within the ARM dataset as homogeneous and plane-parallel (PP) for (a) upwelling TOA shortwave, (b) upwelling TOA longwave, (c) downwelling surface shortwave, and (d) downwelling surface longwave. The legends indicate the means of the error distributions for PP and for plane-parallel calculations with parameterized treatment for inhomogeneity (HI).

plane-parallel calculations, vertical overlap was parameterized using the overcast random method (Stephens et al. 2004). The differences $\varepsilon_{\mathrm{ICA,homog}} = \overline{F}_{\mathrm{ICA,homog}} - \overline{F}_{\mathrm{ICA,inhomog}}$ isolate errors caused solely by assuming horizontal homogeneity, since overlap is exact for ICA calculations, while the differences $\varepsilon_{\mathrm{PP}} = F_{\mathrm{PP}} - \overline{F}_{\mathrm{ICA,inhomog}}$ include errors due to both the overlap assumption and the assumption of horizontal homogeneity. Figure 1 shows a comparison of these differences for Nauru, and other locales are similar. It is apparent that the errors due to the assumption of homogeneity are the primary contributors to the errors in the plane-parallel computations. Table 1 gives mean and root-mean-square values of $\varepsilon_{\mathrm{PP}}$ by locale.

Histograms of $\varepsilon_{\mathrm{PP}}$ for all locales combined are shown in Fig. 2. While a significant number of the domains are well represented by plane-parallel assumptions (i.e., domains with either very small cloud fraction, optically thin clouds, or optically thick horizontally uniform clouds), the errors associated with the remaining population are large. These results illustrate the systematic biases that have been noted previously (Stephens 1988b; Stephens et al. 1991) introduced by treating clouds as homogeneous, namely that shortwave albedo is overestimated and outgoing longwave radiation

TABLE 1. Mean (rms) values of $\varepsilon_{\mathrm{PP}}$ in W m^{-2} by locale: N is the number of domains in each locale, FSDS the downwelling shortwave flux at the surface, FSUT the upwelling shortwave flux at the top of the atmosphere, FLDS the downwelling longwave flux at the surface, FLUT the upwelling longwave flux at the top of the atmosphere; and Sza is solar zenith angle in degrees.

		FSDS		FSUT		FLDS	FLUT
Locale	N	Sza: 20	Sza: 60	Sza: 20	Sza: 60	—	—
Nauru	640	−25.6 (70.3)	−14.6 (35.3)	19.8 (56.3)	12.4 (30.3)	1.54 (3.02)	−2.74 (7.12)
SGP summer	356	−44.7 (109.6)	−22.0 (51.6)	35.1 (87.3)	18.6 (43.6)	2.31 (5.43)	−4.99 (11.7)
SGP winter	468	−62.7 (122.8)	−31.1 (59.2)	49.0 (95.6)	25.3 (48.6)	4.84 (9.30)	−4.07 (7.56)
NSA summer	291	−44.1 (102.5)	−22.1 (49.0)	35.2 (81.5)	18.6 (41.0)	3.54 (8.04)	−2.93 (6.44)
NSA winter	252	−26.0 (67.3)	−14.8 (34.5)	19.2 (50.1)	11.6 (27.1)	3.02 (7.19)	−0.58 (1.46)

TABLE 2. Mean (rms) errors in column radiation budget due to errors in TOA and surface fluxes (ε_{PP}) in W m^{-2} by locale.

Locale	SW, Sza: 20	SW, Sza: 60	LW
Nauru	1.96 (5.46)	0.057 (2.22)	1.20 (5.81)
SGP summer	2.89 (8.52)	0.097 (3.25)	2.69 (7.88)
SGP winter	4.33 (10.8)	1.08 (3.70)	−0.77 (5.47)
NSA summer	2.30 (7.48)	0.18 (2.53)	−0.61 (5.73)
NSA winter	3.01 (7.42)	1.01 (2.42)	−2.44 (6.36)

(OLR) is underestimated. The errors in the top of atmosphere (TOA) and surface fluxes contribute to errors in the radiation budgets for the atmosphere (Table 2). Column shortwave absorption is overestimated by purely plane-parallel calculations. Longwave column flux convergence is overestimated in Nauru and SGP summer, but underestimated in SGP winter, NSA summer, and NSA winter. This difference among the locales appears to be primarily rooted in differences in the downwelling longwave flux at the surface (FLDS, Table 1), with SGP winter, NSA summer, and NSA winter having larger ε_{PP} than do the remaining two locales. Low humidity in the boundary layer and lower troposphere would make FLDS more sensitive to cloud inhomogeneity, suggesting that the errors in the longwave column flux convergence are likely related to differences in the abundance of lower-tropospheric water vapor among the locales.

3. Parameterization for horizontal inhomogeneity

The treatment of horizontal inhomogeneity presented here incorporates covariances between cloud optical properties and the radiance field. The treatment extends the method described by Stephens (1988b) in which the radiative transfer through a heterogeneous medium is characterized in terms of a hierarchy of radiance subgroups with distinct spatial scales. For this work, source terms specific to solar and infrared sources are included. The starting point is the monochromatic equation for three-dimensional radiative transfer with sources:

$$\left[\eta\cos\varphi\frac{\partial}{\partial x}+\eta\sin\varphi\frac{\partial}{\partial y}+\mu\frac{\partial}{\partial z}\right]I(\mathbf{r};\mu,\varphi)=-\sigma_e(\mathbf{r})I(\mathbf{r};\mu,\varphi)+\frac{1}{4\pi}\sigma_s(\mathbf{r})\int_0^{2\pi}\int_{-1}^{1}P(\mathbf{r};\mu,\varphi;\tilde{\mu},\tilde{\varphi})I(\mathbf{r};\mu,\varphi)\,d\tilde{\mu}\,d\tilde{\varphi}$$
$$+(\sigma_e(\mathbf{r})-\sigma_s(\mathbf{r}))B(\mathbf{r};\mu,\varphi), \quad (1)$$

which specifies the radiance $I(\mathbf{r};\mu,\varphi)$ at a point $(\mathbf{r})$ in the direction (θ,φ), where $\mu=\cos\theta$, $\eta=\sin\theta$, $\sigma_e(\mathbf{r})$ is the volume extinction coefficient, $\sigma_s(\mathbf{r})$ is the volume scattering coefficient, $P(\mathbf{r};\mu,\varphi;\tilde{\mu},\tilde{\varphi})$ is the phase function, and $B(\mathbf{r};\mu,\varphi)$ is the Planck emission function.

The domain of interest consists of the cloudy region of a single grid cell in a general circulation model. The in-cloud phase function is assumed to be constant over the domain, while the radiance, volume extinction coefficient, volume scattering coefficient, and blackbody emission function are decomposed into the sum of the domain average and a fluctuation, for example,

$$P(\mathbf{r};\mu,\varphi;\tilde{\mu},\tilde{\varphi})=P(z;\mu,\varphi;\tilde{\mu},\tilde{\varphi}), \quad (2)$$

$$I(\mathbf{r};\mu,\varphi)=\bar{I}(z;\mu,\varphi)+I'(\mathbf{r};\mu,\varphi), \quad (3)$$

$$\sigma_e(\mathbf{r})=\bar{\sigma}_e(z)+\sigma_e'(\mathbf{r}), \quad (4)$$

$$\sigma_s(\mathbf{r})=\bar{\sigma}_s(z)+\sigma_s'(\mathbf{r}), \quad (5)$$

$$B(\mathbf{r};\mu,\varphi)=\bar{B}(z;\mu,\varphi)+B'(\mathbf{r};\mu,\varphi). \quad (6)$$

The blackbody emission function is assumed to be uncorrelated with the intrinsic optical properties. When averaged horizontally,

$$\mu\frac{\partial}{\partial z}\bar{I}(z;\mu,\varphi)=-\bar{\sigma}_e(z)\bar{I}(z;\mu,\varphi)-\overline{\sigma_e'(\mathbf{r})I'(\mathbf{r};\mu,\varphi)}+\frac{1}{4\pi}\bar{\sigma}_s(z)\int_0^{2\pi}\int_{-1}^{1}P(z;\mu,\varphi;\tilde{\mu},\tilde{\varphi})\bar{I}(z;\mu,\varphi)\,d\tilde{\mu}\,d\tilde{\varphi}$$
$$+\frac{1}{4\pi}\int_0^{2\pi}\int_{-1}^{1}P(z;\mu,\varphi;\tilde{\mu},\tilde{\varphi})\overline{\sigma_s'(\mathbf{r})I'(\mathbf{r};\mu,\varphi)}\,d\tilde{\mu}\,d\tilde{\varphi}+(\bar{\sigma}_e(z)-\bar{\sigma}_s(z))\bar{B}(z;\mu,\varphi). \quad (7)$$

The terms $\overline{\sigma_e'(\mathbf{r})I'(\mathbf{r};\mu,\varphi)}$ and $\overline{\sigma_s'(\mathbf{r})I'(\mathbf{r};\mu,\varphi)}$ represent spatial correlations between the optical properties of the domain and the radiance field, and they are taken to be functions of the mean optical properties and radiance field for the domain (Stephens 1988b):

$$\overline{\sigma_e'(\mathbf{r})I'(\mathbf{r};\mu,\varphi)} = \tilde{C}_{eI}(z;\mu,\varphi)\overline{\sigma}_e(z)\bar{I}(z;\mu,\varphi), \quad (8)$$

$$\overline{\sigma_s'(\mathbf{r})I'(\mathbf{r};\mu,\varphi)} = \tilde{C}_{sI}(z;\mu,\varphi)(\mu)\overline{\sigma}_s(z)\bar{I}(z;\mu,\varphi). \quad (9)$$

For flux and heating rate calculations only the azimuthally averaged component of the radiance field is required, and for modeling applications the atmosphere is typically discretized into layers whose optical properties are assumed vertically homogeneous, giving

$$\mu\frac{\partial}{\partial z}\bar{I}(z;\mu) = -\overline{\sigma}_e(1+\tilde{C}_{eI}(\mu))\bar{I}(z;\mu) + \frac{1}{2}\overline{\sigma}_s\int_{-1}^{1}P(\mu;\mu')\bar{I}(z;\mu')\,d\mu' + \frac{1}{2}\overline{\sigma}_s\int_{-1}^{1}P(\mu;\mu')\tilde{C}_{sI}(\mu')\bar{I}(z;\mu')\,d\mu' + (\overline{\sigma}_e-\overline{\sigma}_s)\overline{B}(z;\mu). \quad (10)$$

Insight into the required forms for the correlations can be obtained by transforming the radiative transfer equation into two-stream flux form and examining the expressions for the local reflection and transmission functions. Details of the derivations of the two-stream flux equations are presented in the appendix, and the principal results are summarized here.

Two-stream models

For shortwave transfer, the blackbody emission function is taken to be zero, and the delta-Eddington approximation is used. By requiring that the introduction of horizontal inhomogeneity not introduce directionality in the local reflection and transmission terms, it is found that the correlation functions must be even in μ, and for this work we take them to be constants, represented by the terms C_{eI} and C_{sI} in the following discussion. The resulting flux equation is

$$\frac{d}{d\tau}\begin{bmatrix}F^+(\tau)\\F^-(\tau)\end{bmatrix} = \begin{bmatrix}-(\bar{t}+t') & (\bar{r}+r')\\-(\bar{r}+r') & (\bar{t}+t')\end{bmatrix}\begin{bmatrix}F^+(\tau)\\F^-(\tau)\end{bmatrix} + \begin{bmatrix}Q^+(\tau)\\Q^-(\tau)\end{bmatrix}, \quad (11)$$

where the domain-mean local transmission and reflection, $\bar{t}$ and $\bar{r}$, match the standard delta-Eddington approximations (Meador and Weaver 1980), and the remaining terms are

$$t' = \frac{7}{4}\frac{C_{eI}-f\overline{\omega}C_{sI}}{1-f\overline{\omega}} - \overline{\omega}C_{sI}\left(1+\frac{3}{4}g'\right), \quad (12)$$

$$r' = \frac{1}{4}\left(\frac{C_{eI}-\overline{\omega}fC_{sI}}{1-\overline{\omega}f}\right) - \overline{\omega}C_{sI}\left(1-\frac{3}{4}g'\right), \quad (13)$$

$$Q^+ = -\overline{\omega}\frac{1}{2}(1+C_{sI})\left(1-\frac{3}{2}g'\mu_0\right)\overline{F}_0(\tau), \quad (14)$$

$$Q^- = \overline{\omega}\frac{1}{2}(1+C_{sI})\left(1+\frac{3}{2}g'\mu_0\right)\overline{F}_0(\tau), \quad (15)$$

and

$$\overline{F}_0(\tau) = \overline{F}_0(0)\exp\left[-\frac{1}{\mu_0}\left(1+\frac{C_{eI}-\overline{\omega}fC_{sI}}{1-\overline{\omega}f}\right)\tau\right] = \overline{F}_0(0)\exp[-\kappa\tau], \quad (16)$$

where $g' = g/(1+g)$, $f = g^2$, $\overline{\omega} = \overline{\sigma}_s/\overline{\sigma}_e$, g is the asymmetry parameter, and $\overline{F}_0(0)$ is the flux from the incident collimated beam at TOA.

For longwave fluxes, the constant hemisphere approximation is applied along with the delta-scaled phase function, and the blackbody emission function is taken to be linear in optical depth. The same requirement that the horizontal inhomogeneity not introduce directionality in the local reflection and transmission is applied. The resulting longwave two-stream equation is of the same form as (11) with $\bar{t}$, $\bar{r}$, $Q^+(\tau)$, and $Q^-(\tau)$ matching the standard results for the constant hemisphere approximation (Meador and Weaver 1980) and with

$$t' = -2[C_{eI}-\overline{\omega}C_{sI}\phi], \quad (17)$$

$$r' = -2\overline{\omega}\beta C_{sI}, \quad (18)$$

where $\overline{\omega}$ is as defined in the shortwave case, and β and ϕ are the backscattering and forescattering fractions, respectively. The solution for the shortwave or longwave fluxes then proceeds along standard methods (e.g., Stephens et al. 2001).

4. Effects of correlations on two-stream radiative transfer

These correlations result in a formulation for radiative transfer in which the local reflection, transmission, and shortwave source terms are modified. Fundamentally, a positive correlation between the scattering (extinction) coefficient and the radiance would be expected to enhance scattering (extinction). To the extent that extinction is due to absorption, correlation would also enhance absorption. The effects of the correlations are explored further using a simple single-layer medium. The shortwave model was applied to a conservatively scattering medium of optical depth 5.0 illuminated by a unit flux collimated beam at zenith. The longwave model was applied to an absorbing isother-

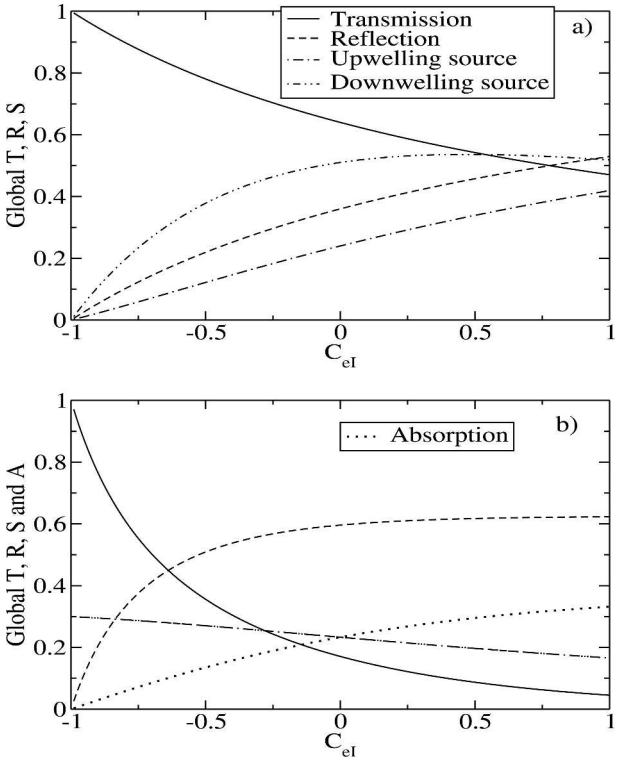

FIG. 3. Variation in transmission, reflection, and sources for a finite layer for (a) shortwave and (b) longwave models as a function of C_{eI}. The shortwave calculations are for a medium with optical depth 5.0, single-scattering albedo 0.999 999 9, and asymmetry parameter 0.85 illuminated from zenith with a direct beam of flux 1.0. The longwave calculations are for a medium with optical depth 15.0, single-scattering albedo 0.99, and asymmetry parameter 0.7 emitting with a uniform blackbody flux of 1.0.

mal medium of optical depth 15.0. The resulting transmissions, reflection, and longwave absorption are shown as a function of C_{eI} in Fig. 3 and behave as expected.

Figure 3 shows that, for a finite layer, increasing C_{eI} causes the shortwave source terms to increase, while the longwave source terms decrease. For the shortwave sources, increasing correlation results in increasing attenuation of the direct beam and, because the medium is conservatively scattering, the attenuated direct flux is converted entirely to diffuse flux. This is evident in Fig. 3, as the sum of the upwelling and downwelling source terms is seen to increase with increasing C_{eI}. Additionally, because of the anisotropic phase function, the source terms are directional and sensitive to the solar zenith angle [see (14) and (15)], causing the downwelling source term to be stronger than the upwelling. As C_{eI} increases, however, scattering increases in this conservatively scattering layer, causing the upwelling and downwelling sources to become almost equal.

In contrast, the longwave sources emit isotropically according to the temperature of the layer. The parameterization assumes that the blackbody emission, a function of temperature, is not correlated with the intrinsic optical properties, and this led to local longwave sources independent of the correlation parameters. However, the transmission is dependent on the correlation parameters and decreases with increasing correlation. Figure 3 indicates that increasing correlation leads to decreased emission from the layer.

To illustrate the limits on values for the correlation parameter in a simple manner, the expression for longwave transfer through a nonscattering, isothermal medium can be examined. For such a layer, the downwelling flux expression can be derived from (10) as

$$F^{-}(\tau) = F^{-}(0)\{\exp[-2(1 + C_{eI})\tau]\} + \frac{B_0}{2(1 + C_{eI})}\{1 - \exp[-2(1 + C_{eI})\tau]\}, \quad (19)$$

where B_0 is as defined in (56). Two features are apparent. First, the case $C_{eI} = -1$ leads to a nonphysical result in which the radiance field is fully decorrelated with the distribution of absorbing/emitting matter in the layer. Second, the case of $C_{eI} < 0$ may in some cases lead to emission in excess of the blackbody emission of the medium. For the expression above, the limiting value of C_{eI} is established by

$$0 \leq \frac{1 - \exp[-2(1 + C_{eI})\tau]}{2(1 + C_{eI})} < 1. \quad (20)$$

For the case of an absorbing and scattering, nonisothermal medium, the limiting values can be evaluated in a similar manner.

For a scattering and absorbing medium, the implication of $C_{eI} > C_{sI}$ is the enhancement of absorption (Fig. 4). For the longwave model, the local t and r may be rewritten from (47) and (48) as

$$t = -2(1 + C_{eI})\left[1 - \overline{\omega}\frac{(1 + C_{sI})}{(1 + C_{eI})}\phi\right], \quad (21)$$

$$r = -2(1 + C_{eI})\overline{\omega}\frac{(1 + C_{sI})}{(1 + C_{eI})}\beta. \quad (22)$$

Thus, the local effect of having $C_{eI} > C_{sI}$ is the rescaling of the single-scattering albedo to a smaller value. A similar rescaling can be demonstrated for the shortwave model.

The case $C_{eI} = C_{sI}$ represents a medium with somewhat specialized properties. Combining (8) and (9) can be shown to give

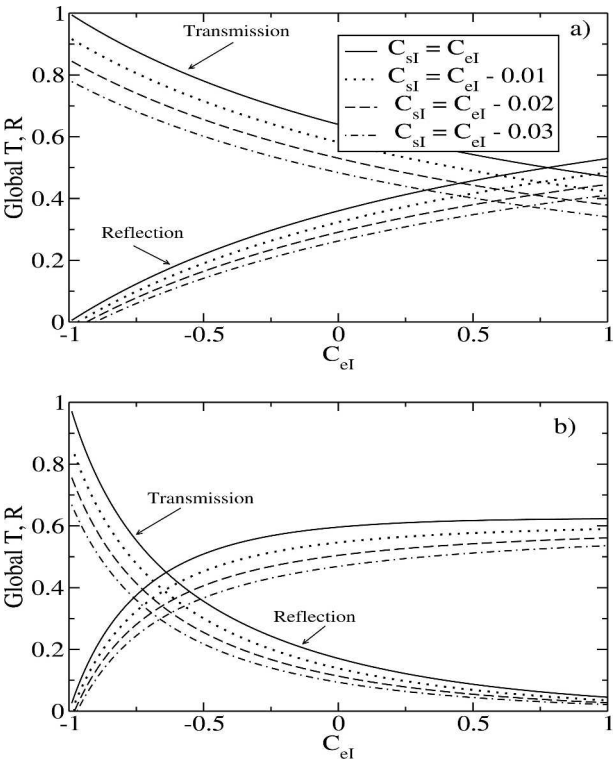

FIG. 4. The effect on global transmission and reflection of $C_{sI} < C_{eI}$ for (a) shortwave and (b) longwave models as a function of C_{eI}. The optical media are as described for Fig. 3. Note that the shortwave results are for a conservatively scattering medium, for which C_{sI} would normally be required to be equal to C_{eI}.

$$\frac{\overline{\sigma}_s(z)}{\overline{\sigma}_e(z)} = \frac{\overline{\sigma_s'(\mathbf{r})I'(\mathbf{r};\,\mu,\,\varphi)}}{\overline{\sigma_e'(\mathbf{r})I'(\mathbf{r};\,\mu,\,\varphi)}} = \frac{\sigma_s'(\mathbf{r})}{\sigma_e'(\mathbf{r})}. \tag{23}$$

Thus, this relationship describes a medium in which the ratio of the fluctuations in the scattering and extinction coefficients is everywhere equal to the ratio of the domain-mean quantities. This relation is trivially satisfied for the case of conservative scattering but, in general, it will be satisfied for any medium for which

$$\sigma_s'(\mathbf{r}) = \frac{\overline{\sigma}_s(z)}{\overline{\sigma}_e(z)}\,\sigma_e'(\mathbf{r}) = \overline{\omega}\sigma_e'(\mathbf{r}). \tag{24}$$

5. Application of the parameterization

The parameters C_{eI} and C_{sI} have been presented as constants for a particular cloudy layer and appear as scalars in the two-stream flux equations. These equations are spectral in that they represent radiative transfer at a particular wavelength, and thus the values for the parameters may vary spectrally. In addition, the values for these parameters would be expected to vary temporally (e.g., during the growth of a particular cloud) and spatially (e.g., vertically within a cloudy column and horizontally between clouds of different types). Within an AGCM exists the flexibility to have these parameters vary spatially and temporally and vary spectrally over the radiative bands used by the AGCM's radiative transfer parameterization. Clearly, however the data required to develop the descriptions of such variations are not yet available. The ARM dataset described earlier does contain information about the appropriate values for these parameters, although with limited sampling in space (three locations) and time (two seasons for two of the locations). A coarse approach to sampling the values for these parameters is to determine their optimum values for each of the locales available in the dataset, and to evaluate the shortwave and longwave values separately.

a. Estimation of required parameters

The new correlation parameterization is implemented in the plane-parallel version of BUGSrad through straightforward changes to the two-stream solver algorithm. The principal changes were adjustments to the expressions for the local transmissions and reflections and, in the shortwave case, the local source terms. For the shortwave solver, the local transmissions and reflections are adjusted for all six bands used by BUGSrad. For the longwave solver, the local transmissions and reflections are adjusted only in the two longwave window bands (800–980 and 1100–1250 cm^{-1}). The effects of cloud inhomogeneity in the longwave are expected to be significant principally in these bands where gaseous absorption is minimal.

For each domain in the ARM dataset, the parameterized version of BUGSrad was used to perform radiative transfer calculation assuming a range of values for C_{eI} and C_{sI} with $C_{eI} \geq -0.95$ and $C_{sI} = C_{eI}$. The results from these calculations were compared with the horizontally inhomogeneous, domain-averaged independent column calculations. For simplicity, the C_{eI} and C_{sI} values were taken to be invariant in the vertical, and only the radiative fluxes exitant from the atmosphere were compared, although conceivably some combination of flux profiles or heating rates could be evaluated. For each exitant flux and each domain, the C_{eI} value that produced minimum bias between the parameterized flux and the independent column flux was determined, providing for each locale and each exitant flux a distribution of best-fit C_{eI} values. Figure 5 shows the biases in heating rates for Nauru for calculations using the simple averages of the best-fit C_{eI} values for the shortwave and longwave fluxes. Improvements in the shortwave and longwave heating rates at TOA and near the surface are apparent and can be attributed to the

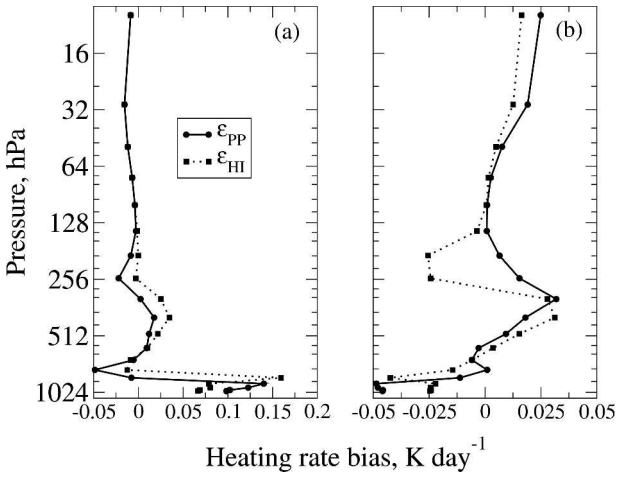

FIG. 5. Biases relative to horizontally inhomogeneous independent column calculations for (a) longwave and (b) shortwave heating rates for Nauru; PP and HI are as defined in Fig. 2.

use of the exitant fluxes to perform the fitting. This figure also suggests that the performance of the parameterization could be improved by allowing the C_{eI} values to vary vertically. The means and standard deviations of the distributions for each locale and each flux are given in Table 3.

Figure 6 shows distributions of the best-fit C_{eI} values for the shortwave and longwave fluxes for Nauru. These values range from 0 to −1 for shortwave and from −1 to 2 for longwave. In general, the shortwave distributions are sharply peaked near zero and are skewed toward negative values. The distribution for the downwelling longwave distributions is somewhat more broadly distributed with a significant number of best-fit C_{eI} values above 1. This might seem to be an error since the implication is that the intrinsic optical properties are more than perfectly correlated with the radiances. However, a central assumption to the derivations was that these correlations were of the forms given by (8) and (9). It seems likely that for these outlying cases the appropriate correlations are not of this form and that the excursion of the correlation parameters to values larger than 1 is a symptom of this lack of fit. It can be

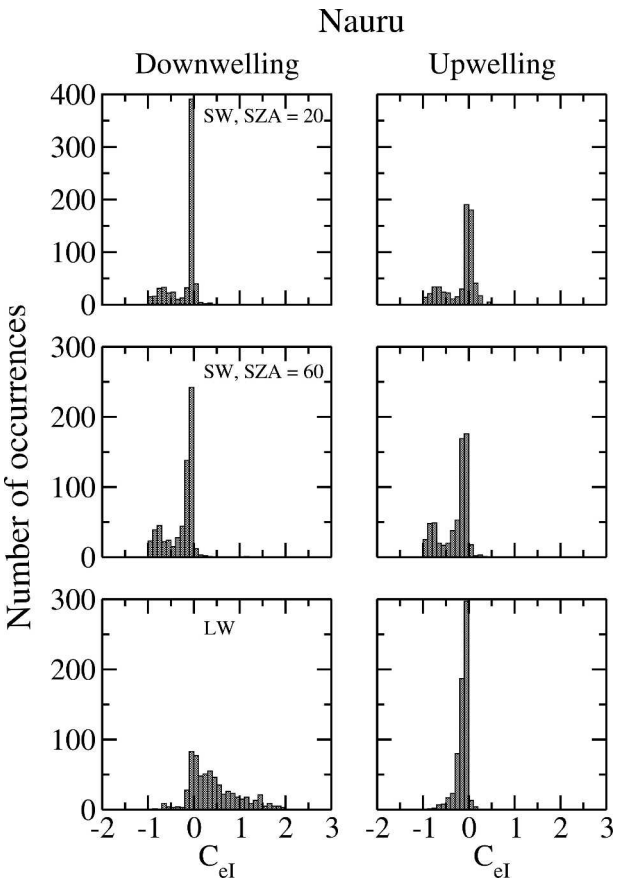

FIG. 6. Distribution of correlation parameter C_{eI}, which produces minimum biases in the exitant atmospheric radiative fluxes for Nauru.

seen in (21) and (22) that values of C_{eI} greater than 1 do not lead to improper values for local t and r and that, in the case of conservative scattering, energy is conserved.

b. Application in an AGCM

A key element in the evaluation of the parameterization is its application to the radiative transfer within an AGCM. BUGSrad has been implemented in the National Center for Atmospheric Research Community Atmospheric Model (CAM; W. D. Collins et al.

TABLE 3. Mean and standard deviation of best-fit C_{eI} values for each exitant flux and locale.

Locale	N	FSDS, 60 $\overline{C_{eI}}(\sigma)$	FSUT, 60 $\overline{C_{eI}}(\sigma)$	FLDS $\overline{C_{eI}}(\sigma)$	FLUT $\overline{C_{eI}}(\sigma)$
Nauru	640	−0.274 (0.299)	−0.301 (0.299)	0.432 (0.529)	−0.143 (0.128)
SGP summer	357	−0.251 (0.337)	−0.229 (0.345)	0.208 (0.445)	−0.190 (0.191)
SGP winter	469	−0.333 (0.337)	−0.328 (0.427)	0.362 (0.634)	−0.173 (0.149)
NSA summer	287	−0.233 (0.325)	−0.230 (0.360)	0.186 (0.520)	−0.123 (0.133)
NSA winter	252	−0.187 (0.211)	−0.196 (0.252)	0.388 (0.638)	−0.080 (0.051)

2003) as part of other work. In principle the values for C_{eI} and C_{sI} could be made functions of cloud type, but for simplicity were specified to be globally uniform with $C_{sI} = C_{eI}$. In the shortwave, the global value for C_{eI} was specified by taking the simple mean over all locales of the best-fit values for the downwelling flux at the surface and upwelling flux at TOA for a solar zenith angle of 60°. The resulting value for C_{eI} was −0.269. In the longwave, there are significant differences in the values of the best-fit C_{eI} for the upwelling and downwelling fluxes, but the longwave fluxes are much less sensitive to C_{eI}. A mean of the values for all the upwelling and downwelling longwave fluxes was used, giving a value of 0.098. These best-fit values for C_{eI} were applied to the domains from the ARM dataset and the resulting errors versus the inhomogeneous ICA calculations were compared with those for standard plane-parallel calculations (Fig. 2). The bias (rms) in the upwelling TOA shortwave improved by 4.6 (5.5) W m^{-2}, and that for the downwelling surface shortwave improved by 6.7 (8.0) W m^{-2}. The bias (rms) in the downwelling surface longwave also improved, by 2.40 (1.61) W m^{-2}, as did that for the upwelling TOA longwave, by 2.34 (1.87) W m^{-2}.

Two AGCM integrations were performed, one with the parameterization (the "test" case) and one (the "control") that used standard plane-parallel BUGSrad. Two-year integrations were performed for each case. Integrations were performed using CAM version 2.0 with specified seasonally varying climatological sea surface temperatures. Differences in the time averages of the model fields for the first two days of the runs give insight into the forcings caused by the horizontal inhomogeneity, while differences in the annual means of the model fields during the last year of the integration provide an understanding of the response of the model. Changes in the radiation budgets for the top-of-atmosphere, surface, and atmosphere are computed as follows. The changes in the net radiative energy into the earth–atmosphere system at TOA and into the earth at the surface are

$$\Delta F_{\mathrm{TOA/SRF;LW/SW}} = F_{\mathrm{net;TOA/SRF;LW/SW;test}} - F_{\mathrm{net;TOA/SRF;LW/SW;control}}, \quad (25)$$

$$\Delta F_{\mathrm{TOA/SRF;net}} = \Delta F_{\mathrm{TOA/SRF;SW}} + \Delta F_{\mathrm{TOA/SRF;LW}}, \quad (26)$$

where the downwelling fluxes at TOA and the surface are positive while upwelling fluxes are negative. The change in the radiative energy into the atmosphere is then

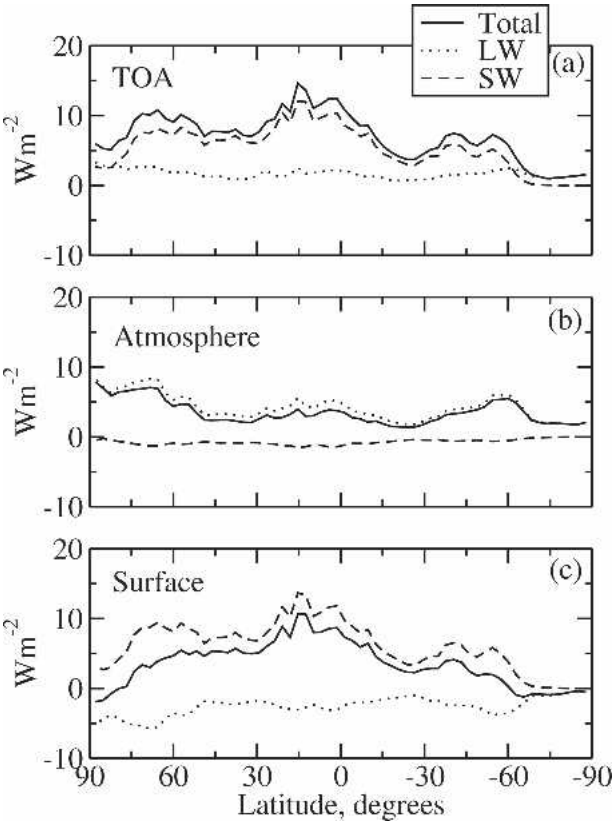

FIG. 7. Time- and zonal-mean radiative budget differences between test and control during the first two days of the AGCM simulations. Budgets are shown for (a) top of atmosphere, (b) atmosphere, and (c) surface and are as defined in Eqs. (25)–(28).

$$\Delta F_{\mathrm{ATM;LW/SW}} = \Delta F_{\mathrm{TOA;LW/SW}} - \Delta F_{\mathrm{SRF;LW/SW}}, \quad (27)$$

$$\Delta F_{\mathrm{ATM;net}} = \Delta F_{\mathrm{ATM;SW}} + \Delta F_{\mathrm{ATM;LW}}. \quad (28)$$

The model integrations begin on 1 September, and over the first two days of the model runs, the impact of introducing horizontal inhomogeneity is much as would be expected based on the single-column single-layer results. Since a negative value of C_{eI} was used for the shortwave component, the cloudy atmosphere is more transparent and less reflective than the equivalent plane-parallel atmosphere. The results (Fig. 7) show an increase in the shortwave flux to the surface, principally occurring in the Tropics and midlatitude storm tracks. A small part of the increase is due to decreased atmospheric absorption (Fig. 7b), and the remainder is due to decreased reflection by clouds. The positive value of C_{eI} used for the longwave component increases the longwave atmospheric flux convergence compared to the plane-parallel case, with decreased longwave emission to space at TOA, and decreased emission to the surface. This result is consistent with (19), which shows

that positive C_{eI} diminishes transmission and diminishes the strength of the source function. At the TOA, the globally averaged total flux input to the earth–atmosphere system has increased by 7.88 W m^{-2}, consisting of a 6.33 W m^{-2} increase in the shortwave flux due to a reduction in planetary albedo and a 1.55 W m^{-2} decrease in the longwave flux to space. At the surface the total flux budget has increased by 4.74 W m^{-2} and is composed of a 7.16 W m^{-2} increase in the shortwave flux and a 2.42 W m^{-2} decrease in the longwave flux.

Regional differences in longwave fluxes occur mainly in the Arctic and subarctic regions due in part to rapid growth of polar clouds over the first days of the model runs (a behavior that occurs in the standard CAM, as well as in the test and control versions of CAM with BUGSrad described here). The total effect on the northern (sunlit) polar surface budget transitions from shortwave-dominated increase in the subarctic to longwave-dominated reduction nearer to the pole. Given the sensitivity of snow and ice cover to surface flux changes, it is expected that the response of the polar regions will be strongly influenced by small changes in the balance between the shortwave and longwave components of the budget.

The annually averaged values from the second year of the model run (Fig. 8) show a similar pattern: enhanced downwelling shortwave flux, a slight decrease in shortwave atmospheric absorption, and reduced longwave emission from the atmosphere. At the TOA, the response of the model has resulted in a globally averaged 7.04 W m^{-2} increase in the total flux input to the earth–atmosphere system, essentially unchanged from the initial state of the model, with a 6.12 W m^{-2} increase in the net shortwave at TOA and a reduction of 0.91 W m^{-2} in the longwave flux to space. The increase is distributed roughly one-third to the atmosphere, driven by a reduction in longwave emission, and two-thirds to the surface, driven by an increase in downwelling shortwave. Over the southern oceans, the shortwave surface fluxes into the surface have increased sharply compared to those of the initial state of the model (Fig. 8c) and are accompanied by a marked decrease in the longwave emission from the atmosphere (Fig. 8b). The globally averaged changes in the radiative budgets for the surface are 6.78 W m^{-2} for the shortwave and -1.54 W m^{-2} for the longwave.

Because these model runs are performed with prescribed sea surface temperatures, the responses of the model are somewhat limited. A more rigorous test of the climatological biases introduced by the assumption of horizontal homogeneity would be obtained by employing a coupled ocean–atmosphere model for these integrations. However, land surface temperatures are free to respond via a coupled land surface model and adjust to values in the range from +7.9 to −3.3 K relative to the control (Fig. 9). Over land surfaces the globally averaged increase in surface temperature is 0.39 K. In the Northern Hemisphere surface warming occurs predominantly in the polar region, in central and north-central Asia, in Siberia, and in eastern North America. The polar warming is strongly associated with reduced cloud cover, with increased column water vapor (CWV) and with reduced shortwave surface albedo. The warming is consistent with reduced occurrence of sea ice in the Arctic Ocean. In Asia, Siberia, and eastern North America the warming is associated with increased CWV, but the influence of cloud amount is less clear than for the polar region. Cooling occurs in the north-central regions of North America and western Europe and is associated with increased cloud cover and increased surface albedo. In the Southern Hemisphere, the Antarctic surface is almost uniformly warmer in spite of only modest increases in downwelling radiative fluxes (Fig. 8) south of 75°S. Cloud

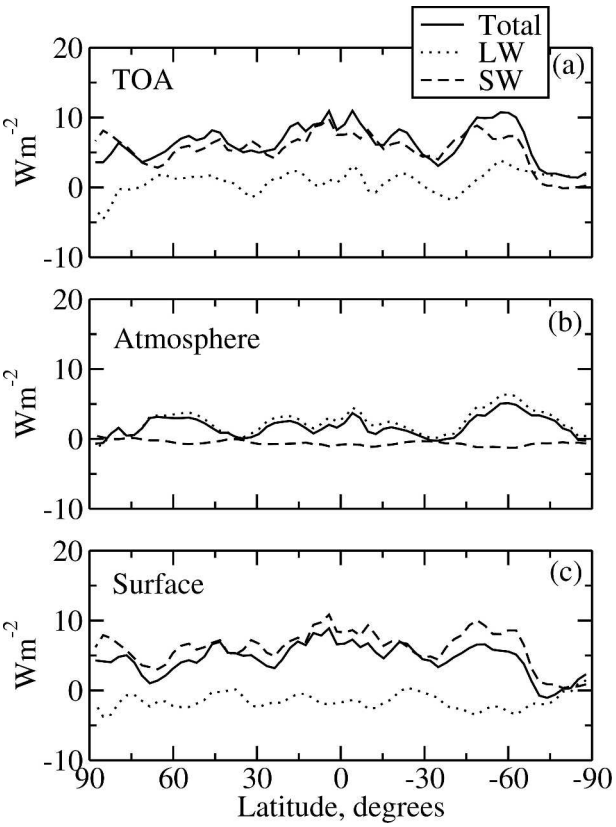

FIG. 8. Time- and zonal-mean radiative budget differences between test and control for the second year of the AGCM run. Budgets are shown for (a) top of atmosphere, (b) atmosphere, and (c) surface and are as defined in Eqs. (25)–(28).

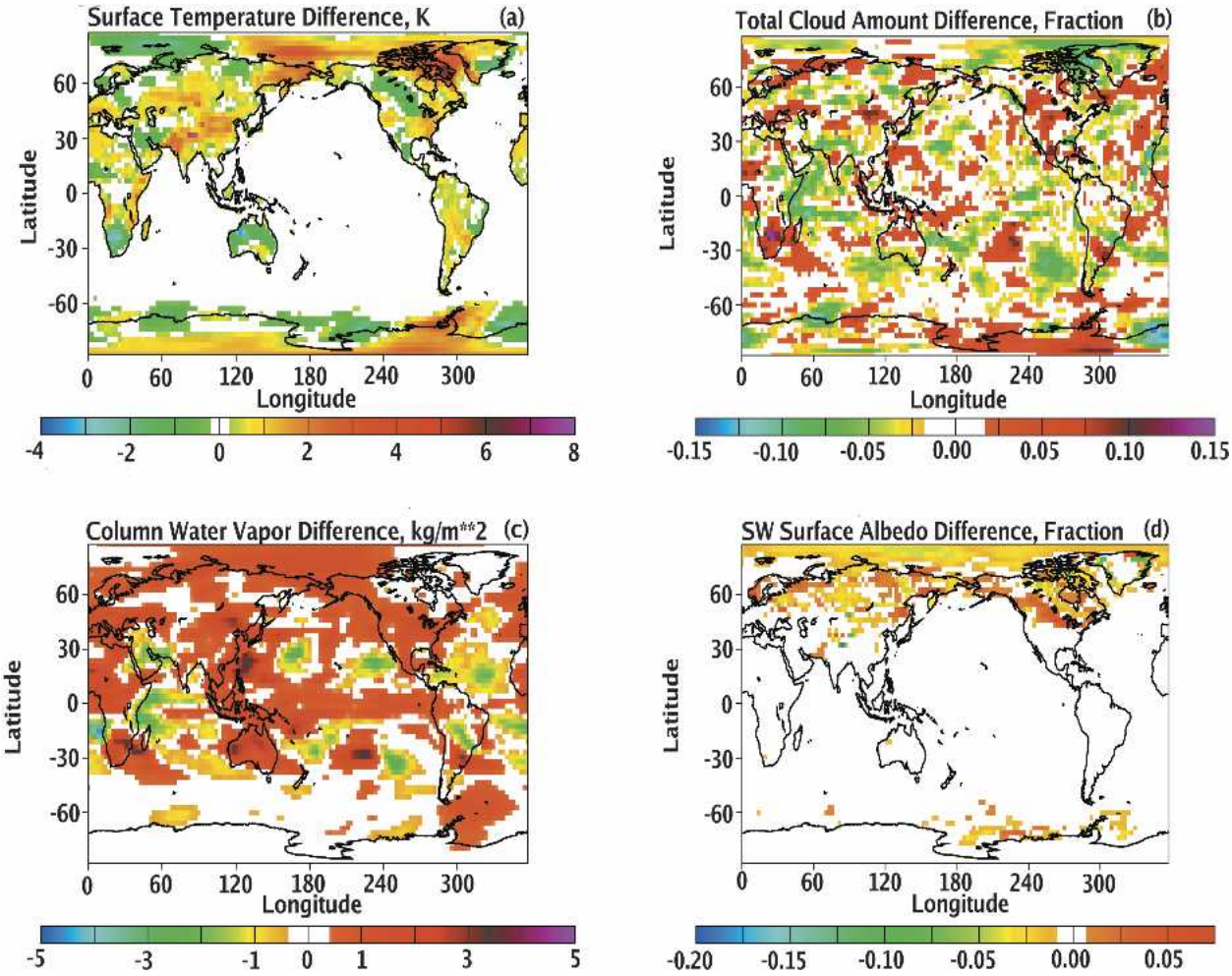

FIG. 9. Response of CAM to horizontal inhomogeneity. Fields are differences (test − control) in annual averages from the second year of the model runs. (a) Difference in surface temperature, (b) difference in total cloud cover, (c) difference in column water vapor, and (d) difference in shortwave surface albedo. Note that sea surface temperatures are fixed.

cover increases over most of western Antarctica, while eastern Antarctica exhibits a mix of increased and decreased cloud cover in various regions. Overall, the polar regions exhibit pronounced sensitivity to the changes induced by cloud inhomogeneity, in large part due to the nonlinear feedbacks associated with snow and ice cover.

6. Summary and conclusions

This work demonstrates a new formulation for the treatment of horizontally inhomogeneous clouds within the framework of one-dimensional radiative transfer. Correlations between the radiance field and the cloud optical properties are treated explicitly within the three-dimensional radiative transfer equation, and the corresponding two-stream equations are derived separately for shortwave and longwave fluxes. Simple single-column, single-layer models are constructed using the formulations and used to demonstrate the effects of correlations on the bulk optical properties of the medium. An established two-stream radiative transfer model is modified to incorporate the formulations, then used along with cloud fields obtained from observational data to estimate required parameters. Finally the model is used as the radiative transfer parameterization within an atmospheric general circulation model. An integration of the AGCM is performed and demonstrates that treating clouds as horizontally homogeneous leads to significant biases in the radiative budgets of the atmosphere and surface. The radiative budget changes contribute to significant surface temperature changes with magnitudes as large as 7.9 K.

A number of issues color the conclusions made here:

- The assumptions about the form of the correlation functions and the appropriate values of the C_{eI} and

C_{sI} coefficients are based on an insufficient sample, both spatially and temporally.
- The horizontal dimension has been proxied by relying on the temporal sampling done by point-based measurement systems.
- Coefficients that almost certainly are dependent on the prevailing convective regime at a particular location have been consolidated into single global values.

All of these issues combine to place large uncertainties on the estimates of the climatological biases induced in AGCM integrations by omitting the treatment of horizontal inhomogeneity within the radiative transfer parameterization. Given the sensitivity of the radiative fluxes, in particular the shortwave fluxes, to horizontal inhomogeneity, it seems necessary to reduce these uncertainties. A number of developments have the potential to improve this situation. First, inasmuch as domain-averaged independent column calculations are more representative of the true radiative transfer within a horizontally inhomogeneous medium (e.g., Zuidema and Evans 1998; Evans 1998), the use of cloud-resolving models (CRMs) as physics parameterizations within AGCMs (Randall et al. 2003) represents an avenue for improvement. However the current computational burdens are too high to allow effective climatological integrations for longer than a few years. Additionally, improvement requires that the CRMs produce the correct horizontal variation in cloud water and ice.

A second avenue lies in the direction of obtaining more complete information about the horizontal variability of cloud water and ice. Not only does this information allow the validation of cloud water distributions produced by cloud-resolving models, but it provides the raw data needed to properly configure the radiative transfer parameterizations, allowing biases to be correctly estimated and corrected. A significant step down this path will be the datasets provided by CloudSat and the Cloud-Aerosol Lidar and Infrared Pathfinder Satellite Observation (CALIPSO; Stephens et al. 2002). The measurements made by these systems will provide data on the horizontal and vertical distributions of cloud condensed water with essentially global coverage for a number of years, providing more fidelity in the parameterization of inhomogeneity within the AGCM. Although the horizontal spatial resolution from CloudSat will be somewhat coarser than has been assumed in this work, the data will be more truly sampled in the spatial domain, as opposed to the proxying approach used here. The issues related to sampling the horizontal subgrid-scale structure at scales of a kilometer as opposed to scales of a few tens of meters will need to be evaluated and addressed. In particular the availability of surface radar and lidar measurements collocated with measurements by the space-based radar and lidar will allow these issues to be addressed.

Acknowledgments. This research was supported by the U.S. Department of Energy, Office of Science, Office of Biological and Environmental Research, Environmental Sciences Division under Grant DE-FG03–94ER61748 as part of the Atmospheric Radiation Measurement (ARM) Program. Data used were obtained from ARM, which is also sponsored by the U.S. Department of Energy, Office of Science, Office of Biological and Environmental Research, Environmental Sciences Division.

APPENDIX

Two-Stream Model

a. Shortwave

Starting from (10), the blackbody emission function is taken to be zero, then the diffuse–direct transformation and delta-Eddington approximations are applied to obtain equations for the upwelling and downwelling diffuse fluxes:

$$\begin{aligned}\frac{\partial}{\partial\tau}\overline{F}^{-}(\tau) = &-\overline{F}^{-}(\tau)\left\{\frac{7}{4}-\overline{\omega}\left(1+\frac{3}{4}g'\right)+\int_{-1}^{0}\left[\left(\frac{\tilde{C}_{eI}(\mu)-\overline{\omega}f\tilde{C}_{sI}(\mu)}{1-\overline{\omega}f}\right)\left(1-\frac{3}{2}\mu\right)\right]d\mu\right.\\ &\left.-\overline{\omega}\int_{-1}^{1}\tilde{C}_{sI}(\mu')\left[\frac{1}{2}-\frac{3}{4}g'\mu'-\frac{3}{4}g'+\frac{9}{8}g'(\mu')^2\right]d\mu'\right\}\\ &-\overline{F}^{+}(\tau)\left\{\frac{1}{4}-\overline{\omega}\left(1-\frac{3}{4}g'\right)+\int_{-1}^{0}\left[\left(\frac{\tilde{C}_{eI}(\mu)-\overline{\omega}f\tilde{C}_{sI}(\mu)}{1-\overline{\omega}f}\right)\left(1+\frac{3}{2}\mu\right)\right]d\mu\right.\\ &\left.-\overline{\omega}\int_{-1}^{1}\tilde{C}_{sI}(\mu')\left[\frac{1}{2}-\frac{3}{4}g'\mu'+\frac{3}{4}g'-\frac{9}{8}g'(\mu')^2\right]d\mu'\right\}+\overline{\omega}\overline{F}_0(\tau)\frac{1}{2}[1+\tilde{C}_{sI}(-\mu_0)]\left(1+\frac{3}{2}g'\mu_0\right),\end{aligned} \tag{A1}$$

$$\frac{\partial}{\partial(-\tau)}\bar{F}^{+}(\tau) = -\bar{F}^{+}(\tau)\left\{\frac{7}{4} - \bar{\omega}\left(1 + \frac{3}{4}g'\right) + \int_{-1}^{0}\left[\left(\frac{\tilde{C}_{eI}(-\mu) - \bar{\omega}f\tilde{C}_{sI}(-\mu)}{1 - \bar{\omega}f}\right)\left(1 - \frac{3}{2}\mu\right)\right]d\mu\right.$$
$$\left. - \bar{\omega}\int_{-1}^{1}\tilde{C}_{sI}(\mu')\left[\frac{1}{2} + \frac{3}{4}g'\mu' + \frac{3}{4}g' + \frac{9}{8}g'(\mu')^2\right]d\mu'\right\} - \bar{F}^{-}(\tau)\left\{\frac{1}{4} - \bar{\omega}\left(1 - \frac{3}{4}g'\right)\right.$$
$$\left. + \int_{-1}^{0}\left[\left(\frac{\tilde{C}_{eI}(-\mu) - \bar{\omega}f\tilde{C}_{sI}(-\mu)}{1 - \bar{\omega}f}\right)\left(1 + \frac{3}{2}\mu\right)\right]d\mu\right.$$
$$\left. - \bar{\omega}\int_{-1}^{1}\tilde{C}_{sI}(\mu')\left[\frac{1}{2} - \frac{3}{4}g'\mu' + \frac{3}{4}g' - \frac{9}{8}g'(\mu')^2\right]d\mu'\right\} + \bar{\omega}\bar{F}_0(\tau)\frac{1}{2}[1 + \tilde{C}_{sI}(-\mu_0)]\left(1 - \frac{3}{2}g'\mu_0\right), \quad \text{(A2)}$$

where $g' = g/(1 + g)$, $f = g^2$, $\bar{\omega} = \bar{\sigma}_s/\bar{\sigma}_e$, $d\tau = -\bar{\sigma}_e(1 - f\bar{\omega})dz$, g is the asymmetry parameter, and $\bar{F}_0(\tau)$ is the flux from the direct beam onto a horizontal surface. The equation for upwelling flux has been modified by applying several variable transformations in order to give it the same sense of flow and integration limits as in the downwelling flux equation. The introduction of horizontal inhomogeneity into a vertically homogeneous medium should not impart a directionality on the local transmission and reflection functions. By inspection of the upwelling and downwelling diffuse flux equations, this can be generally true only if

$$\tilde{C}_{eI}(\mu) = \tilde{C}_{eI}(-\mu), \quad \text{(A3)}$$

$$\tilde{C}_{sI}(\mu) = \tilde{C}_{sI}(-\mu), \quad \text{(A4)}$$

$$\int_{-1}^{1}\tilde{C}_{sI}(\mu')\left[\frac{1}{2} - \frac{3}{4}g'\mu' - \frac{3}{4}g' + \frac{9}{8}g'(\mu')^2\right]d\mu' = \int_{-1}^{1}\tilde{C}_{sI}(\mu')\left[\frac{1}{2} + \frac{3}{4}g'\mu' + \frac{3}{4}g' + \frac{9}{8}g'(\mu')^2\right]d\mu', \quad \text{(A5)}$$

which implies that the correlation functions are even functions of μ. For this work, we take the correlation functions to be constant, which leads to the diffuse and direct two-stream equations

$$\frac{d}{d\tau}\bar{F}^{-}(\tau) = -\bar{F}^{-}(\tau)\left\{\frac{7}{4} - \bar{\omega}\left(1 + \frac{3}{4}g'\right) + \frac{7}{4}\left(\frac{C_{eI} - \bar{\omega}fC_{sI}}{1 - \bar{\omega}f}\right) - \bar{\omega}C_{sI}\left(1 + \frac{3}{4}g'\right)\right\}$$
$$- \bar{F}^{+}(\tau)\left\{\frac{1}{4} - \bar{\omega}\left(1 - \frac{3}{4}g'\right) + \frac{1}{4}\left(\frac{C_{eI} - \bar{\omega}fC_{sI}}{1 - \bar{\omega}f}\right) - \bar{\omega}C_{sI}\left(1 - \frac{3}{4}g'\right)\right\}$$
$$+ \bar{\omega}\bar{F}_0(\tau)\frac{1}{2}[1 + C_{sI}]\left(1 + \frac{3}{2}g'\mu_0\right), \quad \text{(A6)}$$

$$\frac{d}{d\tau}\bar{F}^{+}(\tau) = -\bar{F}^{+}(\tau)\left\{\frac{7}{4} - \bar{\omega}\left(1 + \frac{3}{4}g'\right) + \frac{7}{4}\left(\frac{C_{eI} - \bar{\omega}fC_{sI}}{1 - \bar{\omega}f}\right) - \bar{\omega}C_{sI}\left(1 + \frac{3}{4}g'\right)\right\}$$
$$+ \bar{F}^{-}(\tau)\left\{\frac{1}{4} - \bar{\omega}\left(1 - \frac{3}{4}g'\right) + \frac{1}{4}\left(\frac{C_{eI} - \bar{\omega}fC_{sI}}{1 - \bar{\omega}f}\right) - \bar{\omega}C_{sI}\left(1 - \frac{3}{4}g'\right)\right\}$$
$$- \bar{\omega}\bar{F}_0(\tau)\frac{1}{2}[1 + C_{sI}]\left(1 - \frac{3}{2}g'\mu_0\right), \quad \text{(A7)}$$

$$\bar{F}_0(\tau) = \bar{F}_0(0)\exp\left[-\frac{1}{\mu_0}\left(1 + \frac{C_{eI} - \bar{\omega}fC_{sI}}{1 - \bar{\omega}f}\right)\tau\right] = \bar{F}_0(0)\exp[-\kappa\tau]. \quad \text{(A8)}$$

Define the local transmission, reflection terms, and solar source terms as

$$\bar{t} = \frac{7}{4} - \bar{\omega}\left(1 + \frac{3}{4}g'\right), \quad \text{(A9)}$$

$$\bar{r} = \frac{1}{4} - \bar{\omega}\left(1 - \frac{3}{4}g'\right), \quad \text{(A10)}$$

$$t' = \frac{7}{4}\frac{C_{eI} - f\bar{\omega}C_{sI}}{1 - f\bar{\omega}} - \bar{\omega}C_{sI}\left(1 + \frac{3}{4}g'\right), \quad \text{(A11)}$$

$$r' = \frac{1}{4}\left(\frac{C_{eI} - \bar{\omega}fC_{sI}}{1 - \bar{\omega}f}\right) - \bar{\omega}C_{sI}\left(1 - \frac{3}{4}g'\right), \quad \text{(A12)}$$

$$Q^{+} = -\bar{\omega}\frac{1}{2}(1 + C_{sI})\left(1 - \frac{3}{2}g'\mu_0\right)\bar{F}_0(\tau), \quad \text{(A13)}$$

$$Q^- = \overline{\omega}\frac{1}{2}(1 + C_{sI})\left(1 + \frac{3}{2}g'\mu_0\right)\overline{F}_0(\tau), \tag{A14}$$

and the solar flux equation is written in matrix form as is shown in (11).

b. Longwave

Again starting from (10), the constant hemisphere approximation is applied along with the delta-scaled phase function, leading to

$$\frac{d}{d\tau}\overline{F}^-(\tau) = -2\left[1 - \overline{\omega}\phi + \int_{-1}^{0}\tilde{C}_{eI}(\mu)\,d\mu - \overline{\omega}\frac{1}{2}\int_{-1}^{0}\int_{-1}^{0}\tilde{C}_{sI}(\mu')P(\mu;\mu')\,d\mu'\,d\mu\right]\overline{F}^-(\tau) + 2\overline{\omega}\left(\beta + \frac{1}{2}\int_{-1}^{0}\int_{0}^{1}\tilde{C}_{sI}(\mu')P(\mu;\mu')\,d\mu'\,d\mu\right)\overline{F}^+(\tau) + 2(1 - \overline{\omega})\overline{F}^-_{bb}(\tau) \tag{A15}$$

$$\frac{d}{d(-\tau)}\overline{F}^+(\tau) = -2\left[1 - \overline{\omega}\phi + \int_{-1}^{0}\tilde{C}_{eI}(\mu)\,d\mu - \overline{\omega}\frac{1}{2}\int_{-1}^{0}\int_{-1}^{0}\tilde{C}_{sI}(-\mu')P(\mu;\mu')\,d\mu'\,d\mu\right]\overline{F}^+(\tau) + 2\overline{\omega}\left(\beta + \frac{1}{2}\int_{-1}^{0}\int_{0}^{1}\tilde{C}_{sI}(-\mu')P(\mu;\mu')\,d\mu'\,d\mu\right)\overline{F}^-(\tau) + 2(1 - \overline{\omega})\overline{F}^+_{bb}(\tau), \tag{A16}$$

where $d\tau = -\overline{\sigma}_e dz$, $\overline{\omega} = \overline{\sigma}_s/\overline{\sigma}_e$, $\overline{F}^+_{bb}(\tau)$ and $\overline{F}^-_{bb}(\tau)$ are the upwelling and downwelling blackbody fluxes and

$$\beta = \frac{1}{2}\int_0^1\int_{-1}^0 P(\mu;\mu')\,d\mu'\,d\mu = \frac{1}{2}\int_{-1}^0\int_0^1 P(\mu;\mu')\,d\mu'\,d\mu, \tag{A17}$$

$$\phi = \frac{1}{2}\int_0^1\int_0^1 P(\mu;\mu')\,d\mu'\,d\mu = \frac{1}{2}\int_{-1}^0\int_{-1}^0 P(\mu;\mu')\,d\mu'\,d\mu. \tag{A18}$$

The upwelling flux equation has again been transformed to have the same sense of flow and integration limits as in the downwelling equation. Applying the same requirement that the introduction of horizontal inhomogeneity not impart any directionality into the local reflection and transmission terms again implies that the correlation functions be even function of μ. As for the shortwave, we take the correlation functions to be constant, leading to

$$\frac{d}{d\tau}\overline{F}^-(\tau) = -2[1 - \overline{\omega}\phi + C_{eI} - \overline{\omega}C_{sI}\phi]\overline{F}^-(\tau) + 2\overline{\omega}(\beta + C_{sI}\beta)\overline{F}^+(\tau) + 2(1 - \overline{\omega})\overline{F}^-_{bb}(\tau), \tag{A19}$$

$$\frac{d}{d\tau}\overline{F}^+(\tau) = 2[1 - \overline{\omega}\phi + C_{eI} - \overline{\omega}C_{sI}\phi]\overline{F}^+(\tau) - 2\overline{\omega}(\beta + C_{sI}\beta)\overline{F}^-(\tau) - 2(1 - \overline{\omega})\overline{F}^+_{bb}(\tau). \tag{A20}$$

The evaluation of the integrals defining the forescattering and backscattering fractions requires precise definitions for the integration of the delta function and the Heaviside step function:

$$\int_{x_1}^{x_2}\delta(x - x_0)f(x)\,dx = f(x_0)H(x_2 - x_0) - f(x_0)H(x_1 - x_0), \tag{A21}$$

$$\int_{x_1}^{x_2}H(x - x_0)\,dx = (x_2 - x_0)H(x_2 - x_0) - (x_1 - x_0)H(x_1 - x_0). \tag{A22}$$

Taking the blackbody flux to be linear in optical depth and isotropic, the local transmission, reflection, and longwave source terms become

$$\bar{t} = -2[1 - \overline{\omega}\phi], \tag{A23}$$

$$t' = -2[C_{eI} - \overline{\omega}C_{sI}\phi], \tag{A24}$$

$$\bar{r} = -2\overline{\omega}\beta, \tag{A25}$$

$$r' = -2\overline{\omega}\beta C_{sI}, \tag{A26}$$

$$Q^+(\tau) = 2(1 - \overline{\omega})(B_0 + B_1\tau), \tag{A27}$$

$$Q^-(\tau) = 2(1 - \overline{\omega})(B_0 + B_1\tau), \tag{A28}$$

where B_0 and B_1 are the linear coefficients for the Planck emission as a function of τ. The longwave flux equation can then be written in the form of (11).

With the differential equations for the two-stream shortwave and longwave fluxes defined, the solutions are obtained using standard methods (e.g., Stephens et al. 2001).

REFERENCES

Anasimov, O., and L. Fukshansky, 1992: Stochastic radiation in macroheterogeneous random optical media. *J. Quant. Spectrosc. Radiat. Transfer,* **48,** 169–186.

Barker, H. W., 1996: A parameterization for computing grid-averaged solar fluxes for inhomogeneous marine boundary layer clouds. Part I: Methodology and homogeneous biases. *J. Atmos. Sci.,* **53,** 2289–2303.

Cahalan, R. T., W. Ridgway, W. J. Wiscombe, T. L. Bell, and J. B. Snider, 1994: The albedo of fractal stratocumulus clouds. *J. Atmos. Sci.,* **51,** 2434–2455.

Cairns, B., A. A. Lacis, and B. E. Carlson, 2000: Absorption within inhomogeneous clouds and its parameterization in general circulation models. *J. Atmos. Sci.,* **57,** 700–714.

Clothiaux, E. E., T. P. Ackerman, G. G. Mace, K. P. Moran, R. T. Marchand, M. A. Miller, and B. E. Martner, 2000: Objective determination of cloud heights and radar reflectivities using a combination of active remote sensors at the ARM CART sites. *J. Appl. Meteor.,* **39,** 645–665.

Collins, W. D., and Coauthors, cited 2003: Description of the NCAR Community Atmosphere Model (CAM2). [Available online at http://www.ccsm.ucar.edu/models/atm-cam/docs/cam2.0/description/index.html.]

Dong, X., P. Minnis, G. G. Mace, W. L. Smith Jr., M. Poellot, R. T. Marchand, and A. D. Rapp, 2002: Comparisons of stratus cloud properties deduced from surface, GOES, and aircraft data during the March 2000 ARM cloud IOP. *J. Atmos. Sci.,* **59,** 3265–3284.

Evans, K. F., 1998: The spherical harmonic discrete ordinate method for three-dimensional atmospheric radiative transfer. *J. Atmos. Sci.,* **55,** 429–446.

Gabriel, P. M., and K. F. Evans, 1996: Simple radiative transfer methods for calculating domain-averaged solar fluxes in inhomogeneous clouds. *J. Atmos. Sci.,* **53,** 858–877.

Kato, S., 2003: Computation of domain-averaged shortwave irradiance by a one-dimensional algorithm incorporating correlations between optical thickness and direct incident radiation. *J. Atmos. Sci.,* **60,** 182–193.

Kobayashi, T., 1991: Reflected solar flux for horizontally inhomogeneous atmospheres. *J. Atmos. Sci.,* **48,** 2436–2447.

Meador, W. E., and W. R. Weaver, 1980: Two-stream approximations to radiative transfer in planetary atmospheres: A unified description of existing methods. *J. Atmos. Sci.,* **37,** 630–643.

Oreopoulos, L., and H. W. Barker, 1999: Accounting for subgrid-scale cloud variability in a multi-layer 1D solar radiative transfer algorithm. *Quart. J. Roy. Meteor. Soc.,* **125,** 301–330.

Pincus, R., H. W. Barker, and J.-J. Morcrette, 2003: A fast, flexible, approximate technique for computing radiative transfer in inhomogeneous cloud fields. *J. Geophys. Res.,* **108,** 4376, doi:10.1029/2002JD003322.

Räisänen, P., G. A. Isaac, H. W. Barker, and I. Gultepe, 2003: Solar radiative transfer for stratiform clouds with horizontal variations in liquid-water path and droplet effective radius. *Quart. J. Roy. Meteor. Soc.,* **129,** 2135–2149.

Randall, D., M. Khairoutdinov, A. Arakawa, and W. Grabowski, 2003: Breaking the cloud parameterization deadlock. *Bull. Amer. Meteor. Soc.,* **84,** 1547–1564.

Stephens, G. L., 1978: Radiation profiles in extended water clouds. II: Parameterization schemes. *J. Atmos. Sci.,* **35,** 2123–2132.

——, 1988a: Radiative transfer through arbitrarily shaped optical media. Part I: A general method of solution. *J. Atmos. Sci.,* **45,** 1818–1836.

——, 1988b: Radiative transfer through arbitrarily shaped optical media. Part II: Group theory and simple closures. *J. Atmos. Sci.,* **45,** 1837–1848.

——, P. M. Gabriel, and S.-C. Tsay, 1991: Statistical radiative transport in one-dimensional media and its application to the terrestrial atmosphere. *Transp. Theory Stat. Phys.,* **20,** 139–175.

——, ——, and P. T. Partain, 2001: Parameterization of atmospheric radiative transfer. Part I: Validity of simple models. *J. Atmos. Sci.,* **58,** 3391–3409.

——, and Coauthors, 2002: The CloudSat mission and the A-Train: A new dimension of space-based observations of clouds and precipitation. *Bull. Amer. Meteor. Soc.,* **83,** 1771–1790.

——, N. B. Wood, and P. M. Gabriel, 2004: An assessment of the parameterization of subgrid-scale cloud effects on radiative transfer. Part I: Vertical overlap. *J. Atmos. Sci.,* **61,** 715–732.

Zuidema, P., and K. F. Evans, 1998: On the validity of the independent pixel approximation for boundary layer clouds observed during ASTEX. *J. Geophys. Res.,* **103,** 6059–6074.